Nonlinear Dyn (2025) 113:24383–24404
https://doi.org/10.1007/s11071-025-11401-y

RESEARCH

Characteristics investigation of high speed solenoid valve based on multi-physics co-simulation model

Xiaoming Chen · Yuchuan Zhu · Cheng Qin · Yangmin Li

Received: 9 March 2025 / Accepted: 18 May 2025 / Published online: 12 June 2025

Abstract High speed solenoid valves (HSSVs) serve as indispensable flow modulation component in digital fluid power systems. Their dynamic behavior and identifiability critically depend on characteristic variables derived from coupled electromagnetic, internal fluidic, and mechanical fields. Existing multi-physics models predominantly prioritize the equivalence and verifiability of characteristic variables, while neglecting that distributed internal variables can directly participate in coupling computations through integration, and lack multi-objective optimization opportunities based on high-fidelity correlations between corresponding physical fields and the performance of HSSVs. To address this limitation, this article established a multi-physics co-simulation model for HSSVs. With this framework, the electromagnetic force calculation incorporated magnetic field non-uniformity through finite element analysis. Fluid-dependent forces are resolved using a 3D CFD model with Arbitrary Lagrangian–Eulerian (ALE) meshing, while cross-domain variable coupling is achieved via kinetic equations implemented in MATLAB/Simulink. Validation results demonstrate that the co-simulation model achieves strong agreement with established theoretical models. Electromagnetic force and excitation current predictions exhibit $< 1\%$ deviation from theoretical benchmarks. Pressure oscillation amplitudes maintain $< 3.7\%$ divergence from physical tests, with response time discrepancies confined to 2 ms. Transient flow rate predictions demonstrate 0.08 L/min maximum variance from experimental data. These findings confirm that the proposed multi-physics co-simulation framework effectively captures essential HSSV operational characteristics while providing enhanced physical fidelity over traditional modeling approaches. The developed methodology offers practically relevant design principles that closely align with real-world operating conditions.

Keywords High speed solenoid valve · Electromagnetic force · Fluid-dependent force · Arbitrary Lagrangian–Eulerian (ALE) · Multi-physics · Co-simulation model

X. Chen (✉) · C. Qin
Aviation Industry Corporation of China Xi'an Aircraft Design Institute, Xi'an 710089, China
e-mail: xiaominglut@163.com

X. Chen · Y. Li
Department of Industrial and Systems Engineering, Hong Kong Polytechnic University, Hong Kong 999077, China

Y. Zhu
College of Mechanical and Electrical Engineering, Nanjing University of Aeronautics and Astronautics, Nanjing 210016, China

1 Introduction

Conventional hydraulic components and systems exhibit intrinsic inefficiency due to significant power dissipation through throttling mechanism [1]. A recent

report published by the United States Department of Energy indicates that the mean energy efficiency of hydraulic system remains below 50% [2]. Despite of that, the hydraulic systems are extensively applied in many crucial fields including aerospace, military and industry due to the large weight power ratio and great reliability [3]. Consequently, advancing energy efficiency requires fundamental investigations into fluid dynamic interactions and the development of innovative fluid power architectures. Fortunately, the success of digital electronics strongly motivates the application of digital switching technology in fluid power system, and digitized hydraulic components and systems become efficient and energy-saving gradually [4].

As a crucial control elements in digital fluid power systems, the industrial application of the high speed solenoid valves experiences the barrier that is the insufficient knowledge to the inherent characteristic of high speed solenoid valve and non-instantaneous switching dynamics [5]. Hence, an efficiently and accurately mathematical modelling[1] concerned with the dynamics of high speed solenoid valve is driven by the need for its characteristic evaluation [6]. Note that the dynamics of high speed solenoid valve can be usually represented by the transition events of movable element and is heavily correlated to the drive force terms as forms of electromagnetic force [7] and fluid-dependent force in the kinetic equilibrium equation [8]. Subject to mechanical response, the high speed solenoid valve experiences micro-second response, and the existing control algorithms (such as multiple power sources excitation control strategy [9], intelligent pulse width modulation control algorithm [10,11] and adaptive pre-excitation control algorithm [12,13]) fail to make it switch instantaneously. Hence, the definition and identification of transition events makes it convenient to implement multi-objective optimization of the high speed solenoid valve [14], advantaging its reliability enhancement [15] and ability of fault diagnosis [16].

To acquire the crucial transition events, several non-invasive, non-contact displacement sensing of high speed solenoid valve were proposed by using transient pressure/flow [17], inductance [18], current [19,20] and its derivative [21] identification. The identification accuracy of transition events is governed by the characteristic variables incorporated into multi-physics fields, and multi-physics coupling mechanisms are ultimately manifested through the kinetic equilibrium equations [22]. These representative characteristic variables are electromagnetic force, fluid-dependent force and upstream pressure applied in the equilibrium equation respectively.

Electromagnetic force serves as the primary actuation mechanism in high speed solenoid valves (HSSVs), with its precision control fundamentally relying on comprehensive characterization of governing parameters. Roemer et al. [23] emphasized the dominance of voltage-current relationships in numerical simulations, whereas magnetic circuit geometry effects were unaddressed. In contrast, Yang et al. [24] established structural parameter correlations through steady-state electromagnetic field analyses, yet overlooked dynamic force deviations arising from armature motion-induced flux leakage and magnetic field redistribution.

Except for electromagnetic force, the fluid-dependent force is necessary. Roemer et al. [25] established a transient fluid force model integrating virtual mass, viscous damping, and Basset history terms. Validation via CFD simulations confirmed its accuracy, with prediction errors below 7.5% under operational conditions. However, steady-state fluid-dependent forces exhibit predominant influence over transient flow force in the kinetic equilibrium equations. Meng et al. [26] characterized hydrodynamic forces at varying spool displacements via CFD simulations under the constant supply pressure assumption, while neglecting pressure oscillations induced by high-frequency switching transients in high speed solenoid valves (HSSVs). Wang et al. [27] established frequency-duty cycle matching principles by quantifying pressure oscillation impacts on HSSV performance. Han et al. [28] further demonstrated hydraulic pressure instability through characteristic amplitude/phase analysis of oscillation profiles, revealing coupled effects of supply pressure and orifice opening on upstream oscillations.

While conducting current investigations into electromagnetic forces, fluid-dependent forces and pressure oscillations, several scholars have initiated exploratory efforts in developing multi-physics coupled modeling frameworks. Fang et al. [29] proposed a nonlinear model of an HSV actuator, and three

[1] * Author to whom any correspondence should be addressed. E-mail: xiaominglut@163.com.

subsystems are modeled as a spring/mass/damper system, respectively. Based on a typical equivalent magnetic reluctance model, Gao et al. [30] derived electromagnetic force characteristic equations and established a multi-physics coupled computational model for high speed solenoid valves by integrating steady-state hydrodynamic force equations with ball valve dynamic equilibrium equations. However, conventional theoretical approaches predominantly employ 1D characteristic variables, neglecting the characterization of electromagnetic field distribution and the functional relationship between steady-state hydrodynamic forces and ball valve geometric features were neglected.

Roberts et al. [31] implemented a CFX/Simulink co-simulation for wave energy converters (CFD-modeled buoy hydrodynamics coupled with Simulink-simulated hydraulic control), this methodology effectively resolves cross-domain interaction mechanisms, achieving $< 5\%$ deviation in correlating hydraulic precision with buoy velocity oscillations. Similarly, Yuan et al. [32] employed COMSOL-based ALE mesh deformation to characterize electromagnetic forces and flow rates in proportional valves, utilizing offline look-up tables for multi-physics data exchange with 89.3% interoperability accuracy.

The preceding analysis demonstrated that co-simulation model exhibits unparalleled cross-dimensional coordination and real-time computational capabilities that surpass existing 1D multi-physics models. By incorporating 2D axisymmetric electromagnetic profiles and 3D fluid-dependent force integration into the ball valve kinetic equilibrium equations, this framework enables online feedback of ball valve dynamics to electromagnetic and flow field solvers.

This article is arranged as follow: Sect. 2 presents the structure and principle of high speed solenoid valves (HSSVs) and its experienced multi-physics. The definition of co-simulation model is conducted in Sect. 3. The introduction of the co-simulation method is demonstrated in Sect. 4. Section 5 covers the implementation of co-simulation model. The co-simulation simulation discussion is presented in Sect. 6. Section 7 covers the experimental configuration and discussion. Section 8 summarizes the primary conclusions of this investigation.

2 Structure and principle

The high speed solenoid valve is regarded as a complex apparatus coupled with electromagnetic, mechanic and fluidic fields, and converts the electric energy to mechanical energy. The communication among the multi-physics fields can be accomplished by several variables. The high speed solenoid valve is basically comprised of the armature, excitation coil, static iron, push rod, valve body and ball valve. The schematic diagram of high speed solenoid valve is shown in Fig. 1.

The high speed solenoid valve is actuated by a pulse width modulation (PWM) signal, and experiences periodic opening and closing. When the excitation voltage is exerted on the excitation coil, the generated axial magnetic field distribution enables the ball valve to arrive at the valve seat, blocking the supply flow while connecting the return port to the outlet port. When the excitation coil is de-energized, the ball valve returns to the initial position, blocking the return flow while connecting the supply port to the outlet port. As the movement element, the ball valve is subjected to Newton's second law associated with the electromagnetic force and fluid-dependent force. The transient electromagnetic force depends on the inherent properties of magnets and the distribution related to the geometry of the air gap. The fluid-dependent force incorporated in the CFD model is sensitive to the mesh tolerance and valve opening. These physical fields coupling process are presented in in Fig. 2.

As demonstrated in Fig. 2, the physical fields incorporated in a high speed solenoid valve mainly comprise the electromagnetic, fluidic, and mechanical fields. The communication of multi-physics interactions relies on shared variables across these three fields. The electromagnetic field requires the driving voltage and the ball valve's motion trajectory to account for the effect of the varying air gap on its field distribution. The generated electromagnetic force then serves as input boundary to the mechanical model. The fluidic field requires the ball valve's motion trajectory to determine the fluid-dependent forces at different openings applied in the mechanical model, while the ball valve's displacement derived from the mechanical model provides input boundaries for both the electromagnetic and fluidic fields.

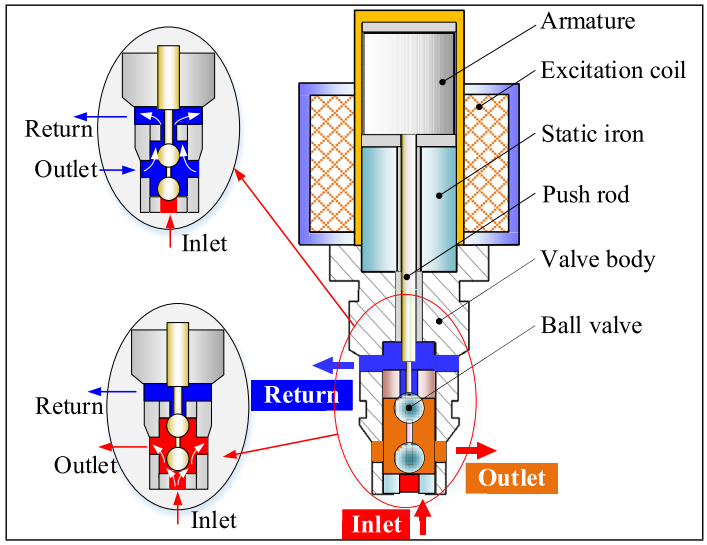

Fig. 1 Schematic diagram of high speed solenoid valve

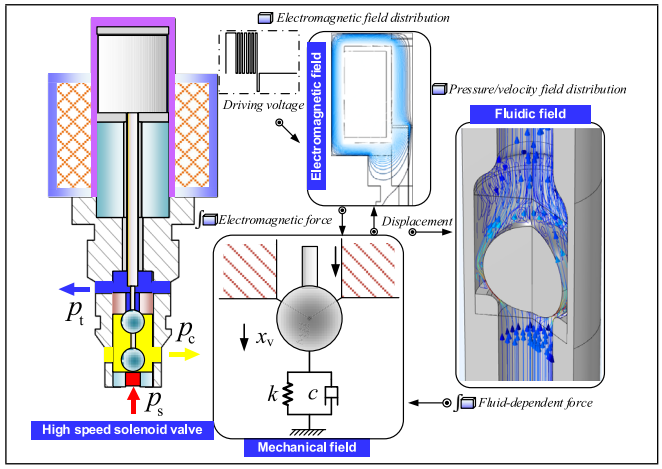

Fig. 2 Communication of multi-physics occurred at HSSV

3 Definition of co-simulation model

Based on the previous discussion of multi-physics fields, this section presents the detailed definition of the co-simulation model. In both the finite element simulation and theoretical models, the communicated variables are defined as 1D time-varying data and ultimately utilized as boundary conditions for computational convenience. Figure 3 illustrates the workflow of the multi-physics co-simulation framework by depicting the interactions between these variables.

As demonstrated in Fig. 3, The 2D axisymmetric electromagnetic field (implemented in COMSOL's electromagnetic module) requires the excitation voltage and the ball valve's motion trajectory. The electromagnetic force, obtained by integrating the magnetic flux density across the air gap, is output as a time-averaged value. The 3D symmetric fluidic field (implemented in the CFD module) requires the ball valve's displacement as an input boundary for the Arbitrary Lagrangian–Eulerian (ALE) meshing method in COMSOL. The calculated electromagnetic force and fluid-dependent force (associated with the ball valve's motion) serve as inputs to the mechanical field governed by the dynamic equilibrium equations. Additionally, the pressure oscillation subsystem incorporates variations in static pressure caused by the delivery flow rate. The inclusion of electromagnetic and fluid-dependent forces ultimately determines the ball valve's motion trajectory through the dynamic

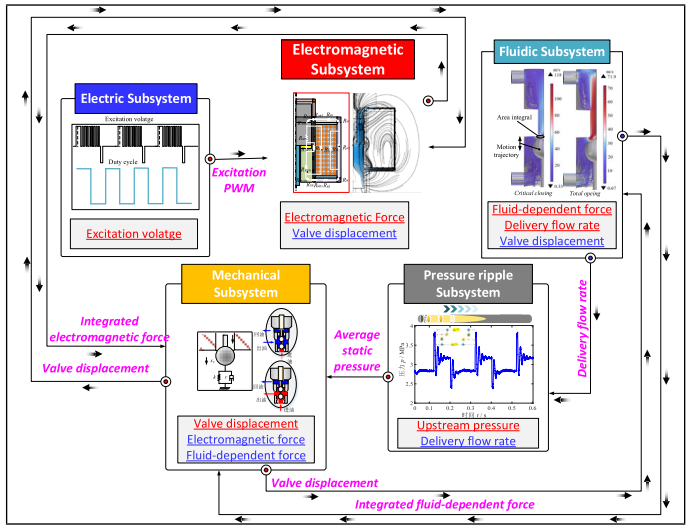

Fig. 3 Flow chart of communicated variables

equilibrium equations. This real-time multi-physics coupling via shared variables provides an efficient method for predicting the dynamic performance of a high speed solenoid valve. To reduce computational complexity and conserve resources, the electromagnetic and fluid-dependent forces are calculated using integral formulations within the finite element model and communicated to the co-simulation framework in real time.

4 Co-simulation method

The co-simulation methodology includes a three-dimensional fluid model to address the fluidic characteristics, a two-dimensional axisymmetric model to capture the electromagnetic field characteristics, a one-dimensional model for calculating the pressure oscillation, and a dynamic equilibrium equation to determine the motion trajectory of the ball valve. These models are linked and co-simulated through an interface implemented by a functional mock-up unit (FMU), defined in accordance with the functional mock-up interface (FMI) standard. The magnetic flux intensity B_g in the air gap is computed via finite element simulation and transmitted to the mechanical dynamics model, which calculates the ball valve displacement x_s and velocity v_s. These computed values are then fed back to the electromagnetic field simulation to update the magnetic flux intensity in the air gap, forming an iterative loop. The ball valve displacement x_s derived from the mechanical dynamic model is transferred to the the CFD model, where the fluid-dependent force is computed and subsequently returned to the mechanical dynamics model. Pressure oscillation modeled with the enhanced transmission line method are provided to the CFD model as inlet boundary condition, while the obtained fluid-dependent force is communicated back to the mechanical dynamic model.

4.1 Electromagnetic equations

Due to the bidirectional coupling between the electric and magnetic fields, the electromagnetic field distribution not only depends on the input boundary conditions and material properties, but is also affected by non-uniformity related to assembly correlations. The challenge of electromagnetic characteristics analysis lies in solving Maxwell's equations under specific boundary conditions, and the static Maxwell's equations are written by the equation:

$$\nabla \times \left(\frac{1}{\mu} \nabla \times \mathbf{A} \right) = J \tag{1}$$

where J is the current density in the excitation coil, μ is the permeability of the material, $\mathbf{A}$ is the magnetic vector potential. It can be helpful to formulate the

magnetic flux intensity B generated by the current in the excitation coil using the magnetic vector potential **A**. This correlation is given by the equation:

$$B = \nabla \times \mathrm{A} \tag{2}$$

The electromagnetic force exerted on the armature can be calculated by integrating the Maxwell's stress tensor over an arbitrary surface S surrounding the armature, as implemented in the COMSOL Multiphysics software:

$$F = \int_S \left[\frac{1}{\mu_0}(\mathbf{B}\cdot\mathbf{n})\mathbf{B} - \frac{1}{2\mu_0}\mathbf{B}^2\cdot\mathbf{n}\right]\mathrm{d}S \tag{3}$$

where S represents the integral surface, and **n** is the magnetic vector. Note that the result of this method is sensitive to the mesh discretization and electromagnetic field distribution.

To implement the numerical simulation of electromagnetic field, several steps are outlined as follows: (1) The static iron and armature are modeled with nonlinear *B-H* curves, and simulated using 'Ampere's Law' nodes. A linear relationship between magnetic flux intensity B and magnetic field intensity H is defined via magnetic permeability, assigned to the media and non-magnetic components. (2) The excitation coil is defined using a 'Multi-Turn Coil' node, where the transient current is determined by the conductivity of the coil material, and the driving voltage acts as a control variable derived from the Simulink model. (3) The Maxwell's Stress Tensor is used to compute the forces on the armature. When applying this method, the mesh around the boundaries should be refined to ensure accuracy. (4) A continuity boundary condition is applied to ensure continuity between the stationary and moving domains. An identity pair is created using 'Form Assembly' feature in the geometric node.

4.2 Fluidic equations

In the fluidic field, the transient flowrate can be obtained associated with the geometric characteristics and status of ball valve accurately. Assuming an incompressible fluid, the continuity equation and Navier–Stokes equation are defined as [33]:

$$\rho_\mathrm{f}\left(\frac{\partial \mathbf{u}}{\partial t} + \mathbf{u}\cdot\nabla u\right) = -\nabla p + \nabla\cdot(\mu_\mathrm{f}(\nabla\mathbf{u} + (\nabla\cdot\mathbf{u})^T) - \frac{2}{3}\mu_\mathrm{f}(\nabla\cdot\mathbf{u})\mathbf{I}) + \mathbf{F} \tag{4}$$

$$\frac{\partial \rho_\mathrm{f}}{\partial t} + \nabla\cdot(\rho_\mathrm{f}\mathbf{u}) = 0 \tag{5}$$

where, **u** denotes the flow velocity, **F** denotes the volume force, ρ_f denotes the fluid density.

The CFD module incorporated in COMSOL Multiphysics software is arranged to calculate the fluid-dependent force and delivery flowrate under the given boundary conditions. To implement CFD simulation, several problems need to be addressed as follow: (1) The ball valve is assumed to be rigid, neglecting the effect of fluid flow. (2) The inlet boundary is defined as inlet conditions with a varying pressure. (3) The mesh surrounding the ball is set to deform freely, following a Yeoh mesh smoothing deformation. The Arbitrary Lagrangian Eulerian (ALE) formulation used for the discretization of the Navier–Stokes equations in a deforming domain is required to the invariant topology of this domain. The mesh displacement is given at the mechanical model. (4) Due to the outlet-side ball is initially forced into contact with valve seat, for the numerical simulation, an offset (10 μm) in the contact settings is needed.

5 Implementation of co-simulation model

In this co-simulation configuration, a fixed time step is applied to both the electromagnetic, fluidic, mechanical model, and the exchange and communication of variables are addressed with the same time interval. The main feature in this co-simulation model is the iterative of variables.

5.1 Electromagnetic field model

The magnetic equivalent circuit (MEC) of high speed solenoid valve is utilized to attain the correct the magnetic flux at the air gap. The magnetic circuit distribution is shown in Fig. 4 and mainly consists of a

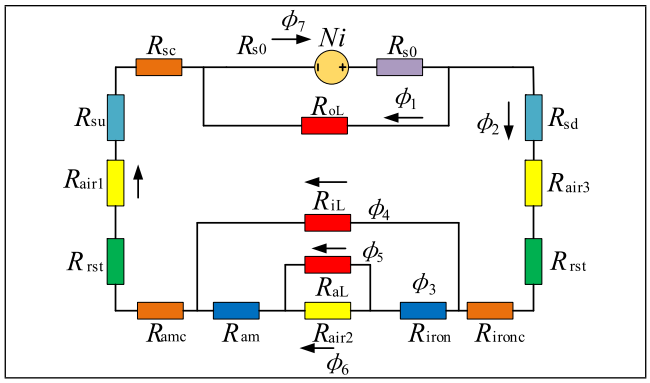

Fig. 4 Magnetic equivalent circuit model of HSSV

nickel steel armature, iron core, stainless steel sleeve, copper coil, nylon frame, magnetic conductive shell, and other components. The high speed solenoid valve contains main magnetic path and three leakage magnetic flux path. The main magnetic circuit is closed magnetic circuit represented by the armature, working air gap, static iron core, shell. The leakage magnetic circuits are represented by the shell leakage reluctance, ϕ_1, ϕ_4, ϕ_6 are the flux leakage reluctance of the excitation coil, armature and iron core, respectively.

As demonstrated in Fig. 4, R_{s0}, R_{am}, R_{air2}, R_{iron}, R_{rst}, R_{air1}, R_{air3}, R_{sc}, R_{amc}, R_{ironc}, R_{su}, R_{sd} represent the shell reluctance, armature reluctance, working air gap reluctance, iron core reluctance, sleeve reluctance, upper radial air gap reluctance, lower radial air gap reluctance, shell corner reluctance, armature corner reluctance, iron core corner reluctance, upper shell radial reluctance and lower shell radial reluctance respectively. R_{oL}, R_{iL}, R_{aL} denote the leakage reluctances of the coil, armature and iron core, and working air gap respectively. The shell reluctance R_{s0}, armature reluctance R_{am}, working air gap reluctance R_{air2} and iron core reluctance R_{iron} are represented by the equations:

$$R_{s0} = \frac{l_{shell}}{\pi(r_{so}^2 - r_{si}^2)\mu_s} \tag{6}$$

$$R_{am} = \frac{l_{am}}{\pi r_{am}^2 \mu_{am}} \tag{7}$$

$$R_{air2} = \frac{\delta}{\pi[r_{am}^2 - (r_{rod} + \delta_{rod})^2]\mu_0} \tag{8}$$

$$R_{iron} = \frac{l_{iron}}{\pi[r_{iron}^2 - (r_{rod} + \delta_{rod})^2]\mu_{iron}} \tag{9}$$

where, l_{shell}, lam, l_{iron} are the height of shell, armature, iron core, δthickness of working air gap, r_{si}, r_{so} are internal and outer radius of shell, r_{am}, r_{iron} are the radius of armature and iron core, r_{rod} is the radius of push rod, δrod is the gap between the push rod and iron core, μ_s, μ_{am}, μ_0, μ_{iron} are the permeabilities of shell, armature, air and iron. The sleeve reluctance R_{rst}, upper radial air gap reluctance R_{air1}, lower radial air gap reluctance R_{air3}, upper shell radial reluctance R_{su} and lower shell radial reluctance R_{sd} are expressed by the equations:

$$R_{rst} = \frac{\ln(\frac{r_{ost}}{r_{ist}})}{2\pi\mu_{st}(l_{su} + l_{sd})} \tag{10}$$

$$R_{air1} = \frac{\ln(\frac{r_{ist}}{r_{am}})}{2\pi\mu_0 l_{su}} \tag{11}$$

$$R_{air3} = \frac{\ln(\frac{r_{ist}}{r_{iron}})}{2\pi\mu_0 l_{sd}} \tag{12}$$

$$R_{su} = \frac{\ln(\frac{r_{si}}{r_{ost}})}{2\pi\mu_s l_{su}} \tag{13}$$

$$R_{sd} = \frac{\ln(\frac{r_{si}}{r_{ost}})}{2\pi\mu_s l_{sd}} \tag{14}$$

where, l_{su}, l_{sd} is thickness of shell upside and downside, r_{ist}, r_{ost}, μ_{st} are internal and outer radius and permeability of sleeve. There is a reluctance appeared at the corner of magnetic element, the corner reluctances of shell, armature and iron core R_{sc}, R_{amc}, R_{ironc} are:

$$R_{\mathrm{sc}} = \frac{1}{8\mu_{\mathrm{s}} r_{\mathrm{so}}} \tag{15}$$

$$R_{\mathrm{amc}} = \frac{1}{4\mu_{\mathrm{am}} r_{\mathrm{am}}} \tag{16}$$

$$R_{\mathrm{ironc}} = \frac{1}{4\mu_{\mathrm{iron}}(r_{\mathrm{iron}} + r_{\mathrm{rod}} + \delta_{\mathrm{rod}})} \tag{17}$$

Combined with the above reluctances, the magnetic equivalent circuit can be represented by below equations group as:

$$\begin{cases} \phi_1 + \phi_2 - \phi_7 = 0 \\ \phi_3 + \phi_4 - \phi_2 = 0 \\ \phi_5 + \phi_6 - \phi_3 = 0 \\ \phi_7 R_{\mathrm{s0}} + \phi_1 R_{\mathrm{oL}} - N_{\mathrm{c}} i = 0 \\ \phi_2(R_{\mathrm{sc}} + R_{\mathrm{sd}} + R_{\mathrm{rst}} + R_{\mathrm{air3}} + R_{\mathrm{ironc}}) \\ \quad + \phi_4 R_{\mathrm{iL}} + \phi_2(R_{\mathrm{su}} + R_{\mathrm{sc}} + R_{\mathrm{air1}} + R_{\mathrm{amc}} + R_{\mathrm{su}}) - \phi_1 R_{\mathrm{oL}} = 0 \\ \phi_3(R_{\mathrm{iron}} + R_{\mathrm{am}}) + \phi_5 R_{\mathrm{aL}} - \phi_4 R_{\mathrm{iL}} = 0 \\ \phi_6 R_{\mathrm{air2}} - \phi_5 R_{\mathrm{aL}} = 0 \end{cases} \tag{18}$$

where, N_{c} is the turns of excitation coil, i is the excitation coil, the flux leakage reluctance R_{oL}, R_{aL}, R_{iL} is identified by the finite element model. Due to the magnetic flux intensity determines the electromagnetic force, the magnetic field intensity at the working gap acts as the output variable in equivalent magnetic model.

The closed magnetic circuit for HSSV is designed to guarantee uniform magnetic field distribution and high magnetic energy efficiency. Based on the rational magnetic circuit architecture, the correlation between the magnetic induction intensity B_{g} and magnetic flux ϕ_6 can be expressed as follows:

$$B_{\mathrm{g}} = \frac{\phi_6}{A_{\mathrm{g}}} \tag{19}$$

where A_{g} refers to the magnetic flux area. Finite element model (FEM) is established to validate the magnetic equivalent circuit, and the magnetic flux intensity at the different air gaps are depicted in Fig. 5.

As demonstrated in Fig. 5, the magnetic flux intensity nonlinearly increases with the decrease of air gap (0.4 mm represents the available air gap is 0.45 mm-0.4 mm), and the predicted by MEC is well agreement with that of FEM.

Thus, the magnetic induction intensity B can be represented by the magnetic field intensity H and

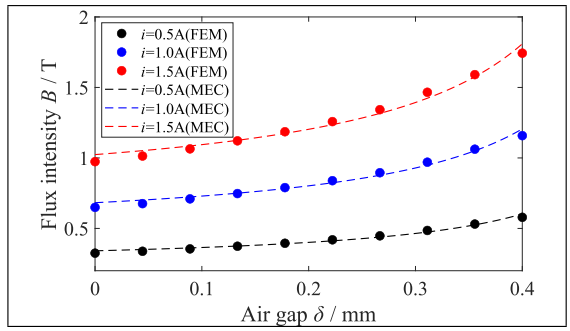

Fig. 5 Steady-state flux intensity at air gap

magnetization intensity M obey the relationship as follows:

$$B = \mu_0(H + M) \tag{20}$$

where μ_0 denotes the air permeability. Here, the magnetic induction intensity seems like dependent on a linear correlation between the magnetic field intensity and magnetization. However, different with nonlinear B–H curve, the magnetization process under axial applied magnetic field is regarded to be a nonlinear phenomenon with magnetic hysteresis.

The magnetic hysteresis derived from the alignment of electron spins into magnetic domains, and the reorganization of such magnetic domains under the effect of an externally applied magnetic field. In the Jiles-Atherton model, each magnetic domain includes a reversible rotation and irreversible rotation, which corresponds to a reversible and irreversible magnetization. Hence, the Jiles-Atherton hysteresis model represented by several parameters exhibits a nonlinear relationship between the variation in the magnetization intensity M and magnetic field intensity H. The effective magnetic field intensity can be written as:

$$H_{\mathrm{eff}} = H + \alpha M \tag{21}$$

where, α is the inter-domain coupling coefficient. The saturation magnetization and domain wall density determine the anhysteretic part of the material behavior, which follows the Langevin function as shown:

$$\mathrm{Lan}(x) = \coth(x) - 1/x \tag{22}$$

This function has a better physical background than the hyperbolic tangent function adapted by the previous studies. The anhysteretic magnetization M_{an} can be written as [34]:

$$M_{an} = M_s \cdot \mathrm{Lan}(a^{-1} \cdot H_{eff}) \frac{H_{eff}}{|H_{eff}|} \tag{23}$$

where, a is the domain wall density, which is characterized by the shape of the anhysteretic magnetization; M_s is the saturation magnetization; H_{eff} is the effective magnetic field intensity. The significant equation in the Jiles-Atherton model determines the variation in the magnetization intensity M caused by the variation in the effective magnetic field intensity H_{eff}, which can be given as [34]:

$$dM = \max(\chi \cdot dH_{eff}, 0) \frac{\chi}{|\chi|} + c_r dM_{an} \tag{24}$$

where, c_r is the magnetization reversibility, which affects the degree of anhysteretic versus hysteretic behavior. If it is set to unity, the model is purely anhysteretic. The auxiliary vector χ is defined as [34]:

$$\chi = k_p^{-1}(M_{an} - M) \tag{25}$$

where, k_p is the domain wall pinning constant, which is applied to controls the pinning and hysteresis of the magnetic moments. The Jiles-Atherton hysteresis model is mainly suitable for time-dependent studies, but it also works in stationary parametric simulation. Several parameters applied to the Jiles-Atherton model is obtained by the parameter identification toolbox in our group's previous works [34].

Therefore, in practical applications, the utilization of the average force by several contours is advised. Based on the magnetic flux intensity distribution, the available electromagnetic force is given by the equation as:

$$F_m = \frac{\psi^2}{2N^2\mu_0 S} = \frac{\phi^2}{2\mu_0 S} = \frac{B_g^2 S_g}{2\mu_0} \tag{26}$$

where, Ψ is the flux linkage, S_g is the magnetic vector area of air gap, N is the turns of excitation coil, μ_0 is the permeability of air, B_g is the average value of the magnetic flux intensity distribution at air gap.

As demonstrated in Fig. 6, the closed magnetic circuit is easy to found. At the initial air gap, the uniform and higher magnetic flux intensity mainly distributed at the static iron core and upper section of armature, and the magnetic flux intensity at the air gap is lower than other section. At the minimal air gap, the reduction of air reluctance enables the higher magnetic flux intensity be distributed at the air gap, which corresponds to higher electromagnetic force.

Based on the nonlinear B–H curve, the closed hysteresis loop curve of magnetic flux intensity in the air gap and its corresponding electromagnetic force is found. The magnetic flux intensity grows at initial air gap slowly, and increases along with the reduction of air gap quickly. At the minimal air gap, the magnetic flux intensity experiences a similar gradient than that of initial air gap due to growth of coil current. That means the magnetic flux intensity is more sensitive to reluctance of air gap rather than the driving current amplitude. The electromagnetic force exerted on the armature follows the similar rule. The apparent turn points appeared at the electromagnetic force curve make it clear that the when to arrange an appropriate driving current to offset fluid-dependent force efficiently.

The correlation between the coil current and magnetic flux intensity at the air gap and electromagnetic force are shown in Fig. 7, respectively.

As demonstrated in Fig. 7, the static electromagnetic force when the working air gaps ranges from the maximum value(δ = 0.45 mm) to minimum value (δ = 0.05 mm) always increases with the growth of excitation current nonlinearly. A larger gradient of electromagnetic force (19N/A) is found at the working air gap of 0.05 mm, and is improved by 23% in comparison with that of the working air gap δ = 0.45 mm. The obtained static electromagnetic force performs as one of the persuasive evidences for the rationality of the designed magnetic circuit of high speed solenoid valve.

5.2 Mechanical field model

The combination of the obtained electromagnetic force and fluid-dependent forces drives the ball valve periodically move. The movement of ball valve can be regarded to be a single-degree freedom mass-damping system, and its momentum equilibrium state is ruled as follow:

$$m_s \frac{d^2 x_s}{dt^2} + b_s \frac{dx_s}{dt} = F_m - F_{st} \tag{27}$$

where, m_s refers to the equivalent mass of mover, b_s refers to the damping coefficient, F_{st} refers to the total force with respect to the fluid.

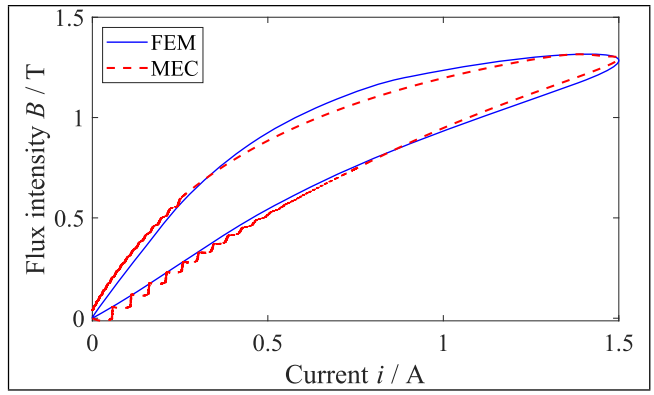

Fig. 6 Comparison of magnetic flux intensity at initial air gaps

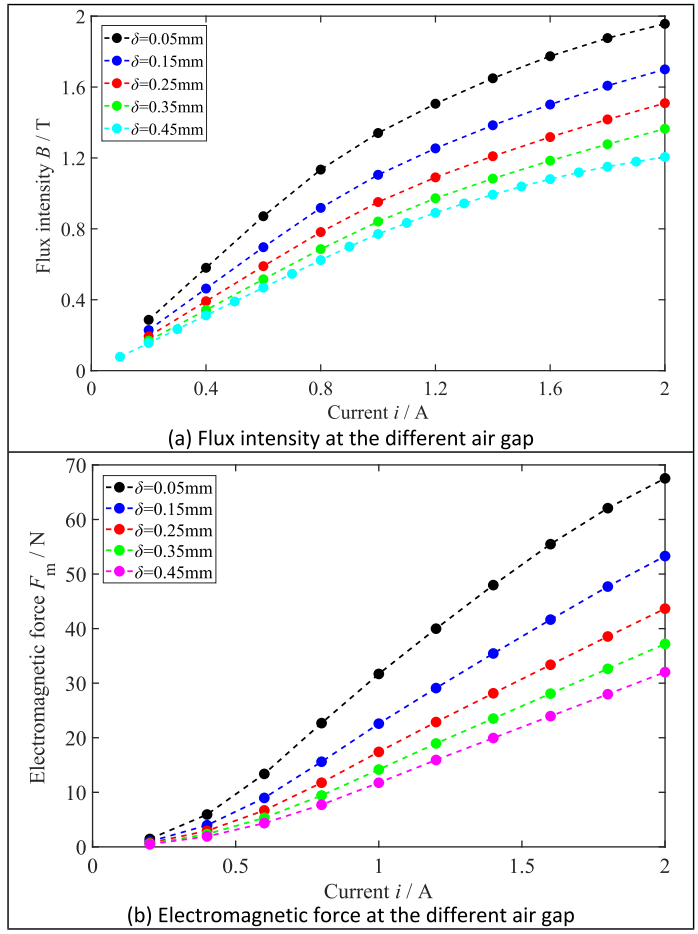

Fig. 7 Magnetic flux intensity and electromagnetic force at the different air gaps

The drag force arises as the valve mover is forced through surrounding viscous fluid. Utilizing a linearized form of the Naiver-Stokes equations, the drag force exerted on a translational sphere immersed in viscous fluid can be given by the equation:

$$m_s = m_v + \frac{2}{3}\rho\pi r_s^3 \tag{28}$$

where, m_v is the mass of movement, ρ is the fluid density, r_s is the radius of ball valve.

5.3 Fluidic field model

The fluid-dependent force varies with the supply pressure and status of ball valve, and is featured by the static pressure, fluid shearing force and flow force etc. Note that total fluid force can be divided into a flow-dependent term (steady flow force) and a motion-dependent term (transient flow force). At non-zero displacement of ball valve, the fluid-dependent force is attributed to the non-uniform pressure distribution on the sphere surface, and can be written as:

$$F_{\text{fluid}} = -\left[p_{\text{d}} + C_{\text{ds}}^2(p_0 - p_{\text{d}})\right]A_{\text{j}}\cos\beta + (p_0 - p_{\text{d}})\left[\frac{2C_{\text{ds}}^2A_{\text{j}}^2}{A_0} + \frac{d_{\text{v}}^2\cos^2\beta}{4} - \frac{C_{\text{ds}}^2\pi d_{\text{v}}x_{\text{s}}\sin 2\beta\cos\beta}{2}\right] \tag{29}$$

where, A_{a} is the pressure shadow area of the valve geometry, A_0 is the entrance area, C_{ds} is the discharge coefficient, p_{d} is the load pressure, p_0 is the supply pressure, d_{v} is the diameter of ball valve, β is the conical seat angle. The flow area A_{j} can be defined as:

$$A_{\text{j}} = \pi x_{\text{s}}\sin 2\alpha_{\text{s}}\left(r_{\text{s}} + \frac{1}{2}x_{\text{s}}\sin\alpha_{\text{s}}\right) \tag{30}$$

where, α_{s} is the half-angle of the valve seat.

To validate the proposed fluid-dependent force model, a three-dimension finite element simulation model of the internal flow field was established. Since having a good convergence, Reynolds-averaged Navier–Stokes (RANS) k-ε turbulence model [35] is widely adopted for numerically calculating the flow field within the hydraulic components, which is also employed here. The momentum, turbulent kinetic, and turbulent dissipation rate are all discretized with defaults value. The boundary conditions (as demonstrated in Fig. 8a) are represented by the pressure-inlet (red zone) at the supply port of 2 MPa, pressure -outlet (blue zone) at the discharge port (ambient pressure), and periodic interior wall conditions acting on the radial section (yellow zone). No-slip wall conditions are set to the other surfaces of the computational domain.

By prescribing reciprocating motion to the outer wall of the ball valve (cyan zone) relying on dynamic mesh methodology, the transient flow characteristics at the different openings (valve displacement ranges from 0 to 0.4 mm) were analyzed. The fluid force was calculated by integrating the transient pressure exerted on the normal surface of ball valve at one reciprocating period. The numerical grid for the chambers and the ducts inside valve chamber is generated by means of Grid Generation Module incorporated into COMSOL software, and the numerical finite element simulation model are shown in Fig. 8b, which provides a view of the hybrid grids configuration.

As demonstrated in Fig. 8, to enhance the accuracy of simulation calculation, the computational fluid domain is divided into regular pie-like structures with different sizes as much as possible, so as to complete the hexahedral meshing. Due to irregular flow areas fails to be meshed by the hexahedral grid, and the custom grid size function has been utilized to refine the grid in the trans-scale areas to ensure an adequate grid size and tolerance where the maximum velocity and pressure gradients occur.

The numerical resolution is affected by the quality of the meshes employed in the CFD simulations. Thus, a grid independence test is conducted by using three different mesh densities, and their total gird is formed by about 19,170, 28,755, 38,340 cells, respectively. The grid independence test is performed at supply pressure p_{s} = 6 MPa and discharge pressure p_{d} = ambient pressure and full stroke of ball valve (0 ∼ 0.4 mm). Due to the barrier of numerical convergence with so many grids, only the fluid phase is considered here while ignoring the cavitation effect inside the valve chamber. The mass flow rate at outlet and fluid-dependent force obtained by using different meshes are compared to each other to estimate the grid dependency of the simulation results, as listed in Table 1.

The computational results converge as the mesh density increases. The maximum relative error of the numerical fluid-dependent force and delivery flow rate at different meshes are 0.49%, 0.44%, respectively. This demonstrates that the influence of grid resolution on the measured variables is negligible. To seek a balance between numerical accuracy and computational costs, Mesh II is selected for the CFD simulations in this study. Figure 9 compares the simulated fluid forces at different valve openings against predictions from the theoretical model during the ball valve core's motion.

As illustrated in Fig. 9, the ball valve stay at the initial valve opening of 0.05 mm due to maintain flow continuity. Meanwhile, the valve port is reliably closed under the action of spring force, and the

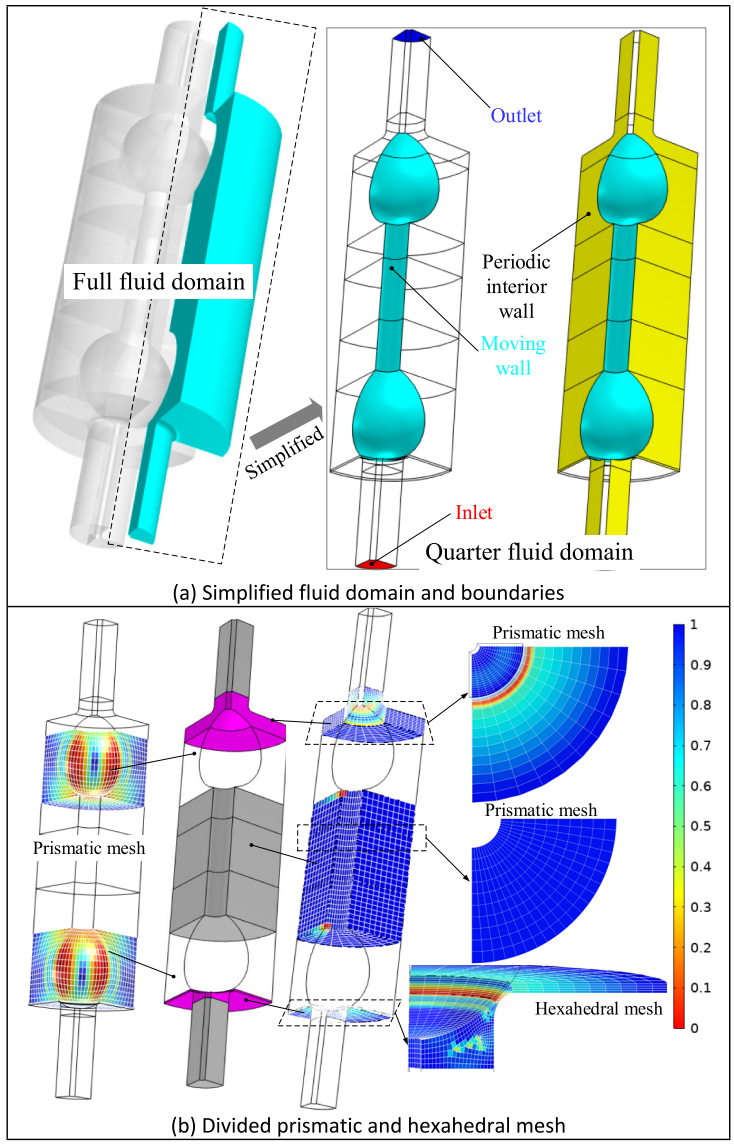

Fig. 8 Definition and meshing of fluid domain

hydrodynamic force, which is mainly manifested as a static pressure force. The simulated and theoretical static pressure force are 7.75N and 7.65N, respectively, and their difference is 1.2%. Under the combined action of electromagnetic force and spring force, along with the increase of valve opening, the area of static pressure slightly reduces, and the proportion of hydrodynamic force is gradually increased. The steady-state hydrodynamic force arrives at 0.65 N (static pressure force changes from 7.75N to 7.1N), accounting for only 8.4% of the normal static pressure force. The maximum error between the finite element simulation results and the theoretical prediction is 4.4%, which indicates that the proposed theoretical model can basically describe the variation law of the steady-state hydrodynamic force at the valve port during the movement of the ball valve.

Theoretically, the delivery flow of high speed solenoid valve is correlated to the status of flow divided into the turbulent and laminar flow. Even the opening is fixed, the valve still experiences the time-varying pressure differential, causing the notable variation of flow characteristic. To account for this variation, the calculations of leakage and correction of discharge coefficient are needed. The flow

Table 1 Comparative results at different meshes

Mesh type	Cells	Fluid dependent force (N)			Maximum Error
		0.2 mm	0.3 mm	0.4 mm	
Mesh I	19,170	3.486	3.232	2.757	0.49%
Mesh II	28,755	3.469	3.217	2.765	
Mesh III	38,340	3.486	3.218	2.767	
Mesh type	Cells	Delivery flow rate (L/min)			Maximum error
		0.2 mm	0.3 mm	0.4 mm	
Mesh I	19,170	0.872	0.249	0.0952	0.44%
Mesh II	28,755	0.877	0.249	0.099	
Mesh III	38,340	0.878	0.247	0.1007	

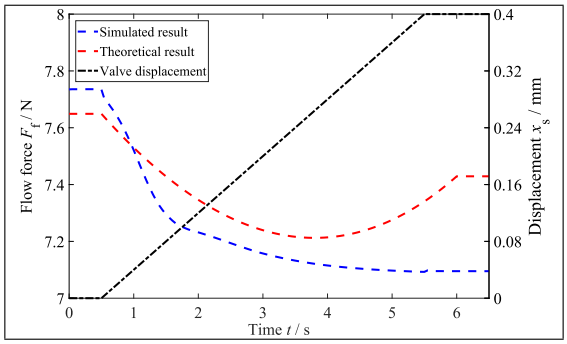

Fig. 9 Flow force at the different displacement

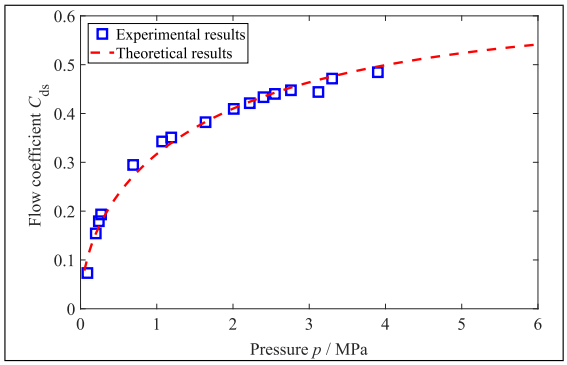

Fig. 10 Discharge coefficient at different supply pressure

coefficient C_{ds} varied with the growth of available pressure differential Δp_{sv}, and subjected to the critical flow number Re_{crit}. The correct flow coefficient C_{ds} can be given by the equation:

$$C_{ds} = C_{dsmax} \tanh\left(\frac{2\mathrm{Re}}{\mathrm{Re}_{crit}}\right) \tag{31}$$

$$\mathrm{Re} = \frac{\rho d_h}{\mu}\sqrt{\frac{2\Delta p_{sv}}{\rho}} \tag{32}$$

where Re_{crit} is the critical flow number, C_{dsmax} is the maximum flow coefficient, d_h is the hydraulic diameter.

As illustrated in Fig. 10, the experimental flow coefficient is basically consistent with the theoretical results at the different supply pressures. The flow coefficient at supply pressure of 4 MPa is 1.7 times that at the supply pressure of 1 MPa, which results in the lower supply pressure experiences less flowrate even the invariant flow area.

5.4 Pressure oscillation model

As a disturbance of dynamic momentum equilibrium of ball valve, the pressure wave propagation effect within complex flow path heavily affects the valve's upstream or downstream pressure. The transmission line (TLM) is viewed as an efficient solution to model the pressure and/or flows at the inlet and outlet only using a number of linear transfer functions and pure time delays. This methodology is originally proposed by Krus et al.[36], whose model of a uniform cross-sectional tube featured by the simplified friction model, which is improved by Johnston [37]. Wiens et al. expanded the objective of this model to the linearly taper tube with the improved accuracy and wider range of applicability [38].

In reality, the flow path (they function as transmission lines, and are similar to tubes) located at the downstream of fast switching valve is uniform cross-sectional area. Fortunately, Wiens realized that using a

number of piecewise linearly tapered segments to model a sufficient long tube with arbitrary cross-sectional area. The main purpose of this work is modeled the geometry-dependent pressure wave propagation effect at downstream of high speed on off valve accurately, which is an essential condition to design a suitable controller for the high speed on off valve with less energy loss. Besides, the preliminary researches by the Wiens indicates that an inertance tube with a changing cross section can be exploited to provide higher energy efficiency than a typical tube of constant radius. The layout of arbitrary radius flow path and TLM of a tapered tube are shown in Fig. 11.

As demonstrated in Fig. 11, the $G(s)$ transfer functions are represented by a sum of parametric first-order transfer functions, and $H(s)$ function is represented by a sum of parametric decaying exponentials. These parameters can be tabulated as functions of the taper ratio and the dissipation number, given by [38]:

$$\lambda_{\mathrm{A}} = \frac{r_{\mathrm{B}}}{r_{\mathrm{A}}} \tag{33}$$

$$\beta = \frac{\upsilon l_{\mathrm{t}}}{c r_{\mathrm{A}}} \frac{(1 + \lambda_{\mathrm{A}} + \lambda_{\mathrm{A}}^2)}{9\lambda_{\mathrm{A}}^3} \tag{34}$$

where, r_{A} and r_{B} are the radius of flow path at inlet and outlet, l_{t} is the axial length. Other parameters that applied to the model are the wave propagation time, given by

$$T = \frac{l_{\mathrm{t}}}{c} \tag{35}$$

And the characteristic impedance:

$$Z_{\mathrm{c}}(x) = \frac{\rho c}{A(x)} \tag{36}$$

where Z_{CA} and Z_{CB} are the impedances at the inlet and outlet. The TLM structure contains linear transfer functions E(s), F(s), and G(s) which are arranged in the configuration shown in Fig. 11(b), and are defined by the weighting functions as follows [38]:

$$F(s) = Z_{\mathrm{c}} + bE(s) \tag{37}$$

$$b = 1 - \frac{8\beta}{\sum_{i=1}^{k} \frac{m_{Ei}}{n_i}} \tag{38}$$

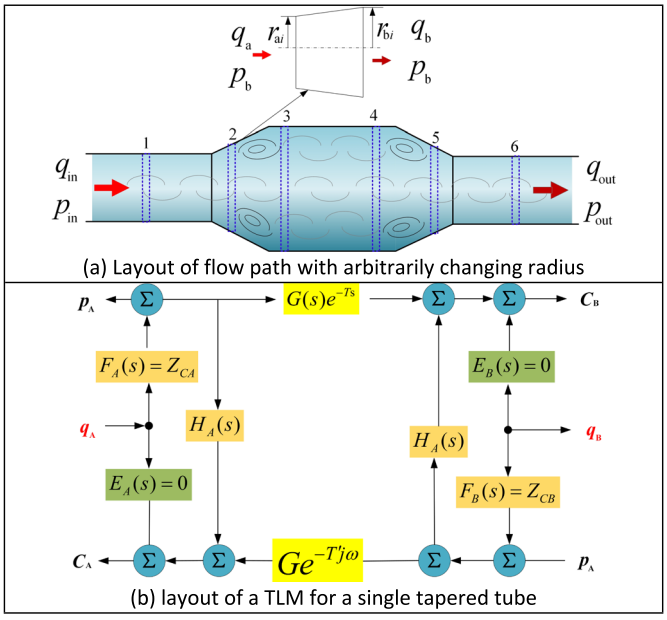

Fig. 11 Schematic of arbitrary shaped flow path

$$G(s) = 1 - \sum_{i=1}^{k} \frac{m_{Gi} Ts}{n_i + Ts} \tag{39}$$

$$T' = \tau T = \tau \frac{l}{c_e} \tag{40}$$

where m_{Gi}, m_{Ei} and τ are the weighting factors; F(s) is scaled off of the E(s) transfer function. This gives the model the ability to accurately calculate the pressure drop during steady-state conditions. The weighting factors n_i are given as follow:

$$n_i = \frac{0.3}{1 + 3\beta}, \quad n_{i+1} = 3n_i \tag{41}$$

Note that, better results were obtained by slightly modifying the wave propagation time T by a factor τ. Besides, the inputs and outputs of the single TLM can be selected by the algebraically solving the characteristic equations for either or flow

$$C_A = p_A - q_A Z_{CA} \tag{42}$$

$$C_B = p_B - q_B Z_{CB} \tag{43}$$

where, C_A and C_B are the constant, Z_{CA} and Z_{BC} are the inlet and outlet impedance, respectively. As mentioned early, an arbitrarily shaped flow path can be modeled by the combination of linearly tapered segments. Hence each segment corresponds to specific dissipation number and taper ratio.

To declare the influence of the pulsation supply pressure on the delivery flowrate, combined with Eqs. (33)–(43), the acquired steady-state flowrate is depicted in Fig. 12.

As depicted in Fig. 12, with growth of duty cycle, the steady state flowrate at condition of constant supply pressure approximately linear increase, and the linearity of delivery flowrate is a little worse. The pulsation of supply pressure causes the difference of 0.076L/min can be found, compared with that of the constant supply pressure.

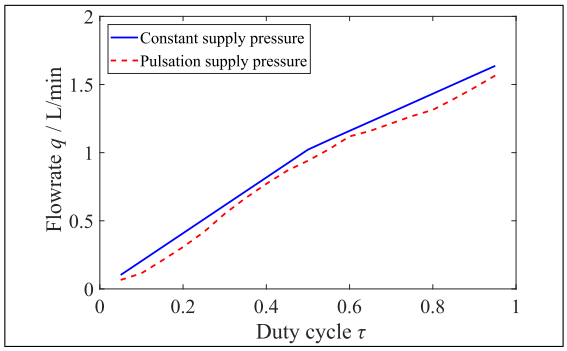

Fig. 12 Affection of pulsation supply pressure on flowrate

6 Co-simulation simulation discussion

Based on the electromagnetic field model, mechanical field model, fluidic field model and pressure oscillation model, the co-simulation model is built in the MATLAB platform. The acquired main parameters in co-simulation model are listed in Table 2.

Since my model establishes a two-dimensional simulation model, compared with the theoretical model, it can not only reflect the thickness of the air gap, but also take into account the influence of the shape characteristics of the air gap on the electromagnetic field, and the electromagnetic characteristic results are more accurate. The acquired excitation current and electromagnetic force at the different profile of air gap is depicted in Fig. 13.

As depicted in Fig. 13, in the excitation duration, the electromagnetic force obtained by air gap ① is consistent with that of air gap ②, and the profiles of air gap has no influence on the electromagnetic distribution when the solenoid actuator experiences the reduction of air gap. In the no energized duration, the electromagnetic force associated with air gap ① is lower than that of air gap ②. The increased air gap has heavy influence on the reduction of electromagnetic force. The finite simulation model can characterize the effects of air gap outer contour variations on transient excitation current and electromagnetic force while maintaining constant characteristic dimensions of the air gap, demonstrating the significance of accounting for distribution characteristics. To evaluation the accuracy of co-simulation model conveniently, the corresponding theoretical model is established, and the characteristics comparison between the co-simulation model and theoretical model under the same conditions as depicted in Fig. 14.

As illustrated in Fig. 14, the coil current calculated by the co-simulation model is consistent with that of theoretical model, the maximum tolerance of total opening current and time are 14% and 0.6%, respectively; the maximum tolerance of total closing current and time are 5.1% and 0.4%, respectively. The

Table 2 Main parameters for co-simulation model

Number	Properties	Units	Value
1	Coil resistance	R	10.2 Ω
2	Polarization area	S	48×10^{-6} m^2
3	Air permeability	μ_0	$4\pi \times 10^{-7}$ H/m
4	Coil turns	N	900
5	Supply voltage	V_e	24 V
6	Axial air gap for armature	δ_0	0.45×10^{-3} m
7	Diameter of orifice	d_s	1.4×10^{-3} m
8	Diameter of ball valve	d_v	2.4×10^{-3} m
9	Radius of valve chamber	r_b	5.0×10^{-3} m
10	Mass of mover	m_v	0.014 kg
12	Radius of flow path	r_t	0.002 m
13	Length of flow path	l_t	0.005 m
14	Dynamic viscosity of fluid	μ	0.0279 Pa s
15	Wave propagation speed	c	1300 m/s
16	Kinematic viscosity of fluid	υ	32×10^{-3} m^2/s
17	Density of fluid	ρ	880 kg/m^3
18	Damping coefficient	b_s	0.6 N s/m
19	Radius of ball valve	r_s	1.2×10^{-3} m
20	Maximum discharge coefficient	C_{dsmax}	0.49
21	Hydraulic diameter	d_h	1.15×10^{-3} m
22	Critical flow number	Re_{crit}	2750

difference indicated that the leakage magnetic associated with the assembly correlation is incorporated into the co-simulation model. The acquired transient current by co-simulation model is consistent with that of theoretical model, and the larger error is found due to the of nonlinear magnetization heavily dependent on the interpolation B–H curve rather than the double curved straight curves.

To validation co-simulation model can describe the pressure oscillation characteristic at the downstream of high speed solenoid valve well, the validated theoretical model is arranged to compare it. The delivery flowrates calculated by the co-simulated model and validated theoretical model are shown in Fig. 15.

As depicted in Fig. 15, during the single switched period, the pulsation of supply pressure enables the unsteady delivery flowrate, and the error between the theoretical model and simulated model is 0.05L/min.

7 Experimental configuration and discussion

To validate the proposed multi-physics co-simulation model, the test platform and results are discussed in this section. The coil current, upstream pressure response and transient flow rate are used to evaluate the accuracy of the proposed co-simulation model in analyzing the electromagnetic characteristics, flow field characteristics, and dynamic characteristics of the high speed solenoid valve.

7.1 Experimental configuration

As demonstrated in Fig. 16, it is mostly comprised of the measured 2/3 way high speed solenoid valve, RT-Link target controller, and hydraulic power unit. The RT-Link target controller consists of a master and slave computer, data acquisition card (NI PCI 6259) and a power amplifier (LYB-305D, Response frequency: 20 kHz, Maximum voltage: ± 30 V) arranged to supply sufficient control voltage. The

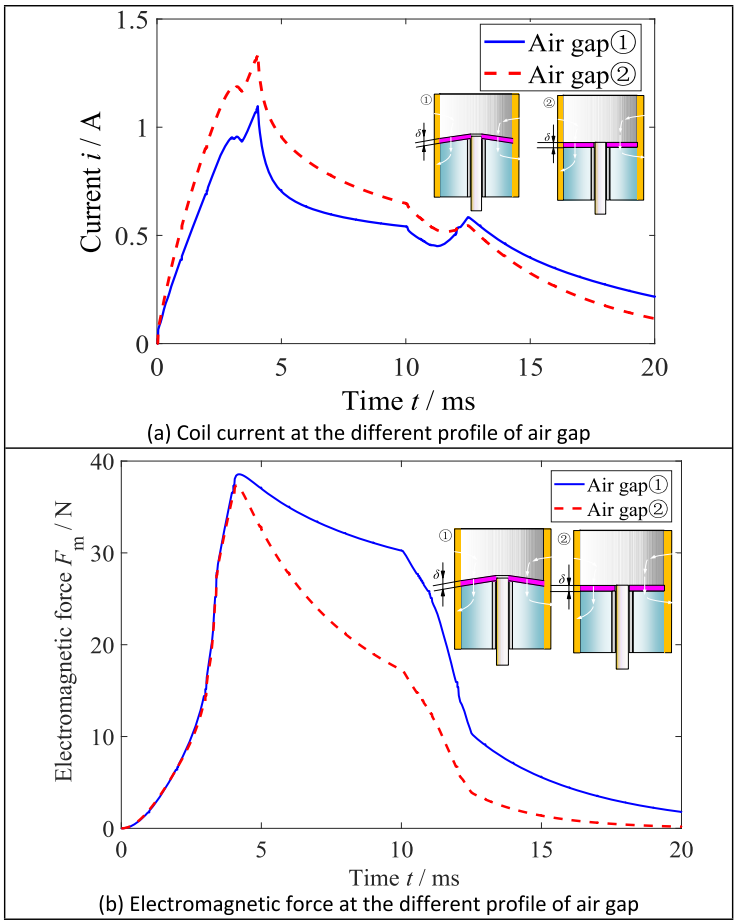

Fig. 13 Characteristics estimated by Co-simulation model at the different conditions

measure platform contains the non-contact current sensor (Shenzhen Zhiyong, CP8000, bandwidth of 50 MHz, rising time of less than 7 ns, range 0.1 $\sim$ 30A) applied to measure the coil current of the measured valve, the high frequency pressure sensor (Kunshan Shuanqiao CYG1401F, accuracy 0.5%, response frequency 20 kHz, range 0 $\sim$ 10 MPa) used to measure dynamic pressure and a gear flowmeter (range 0.02-3L/min, nonlinear tolerance $\leq \pm$ 0.5%) is applied to capture the transient state flow rate. All of the measure apparatus mentioned previously is powered by a linear DC power supplier (Chaoyang Power 4NIC-X24, output power 24 V, and ripple wave less than 1 mV). Initially, the data derived from transient pressure and coil current are collected and transferred to the PCI 6259 through the differential transfer module.

7.2 Characteristics discussion

Combined with the transient current and pressure response, the crucial status of high speed solenoid valve can be estimated relying on the proposed co-simulated model. The experimental configuration as demonstrated in Fig. 16 with function of capture the transient current and pressure oscillation. To validate the accuracy of co-simulation model established in this article, the comparison between the calculated transient current curve and that of measured is depicted in Fig. 17.

As demonstrated in Fig. 17, Under dual-voltage PWM driving, during the coil current rise phase, the experimentally measured transient coil current curve exhibits a spike (where the current initially decreases and then increases), which is in good agreement with the co-simulation model. However, the measured coil current shows a higher rate when the valve core is

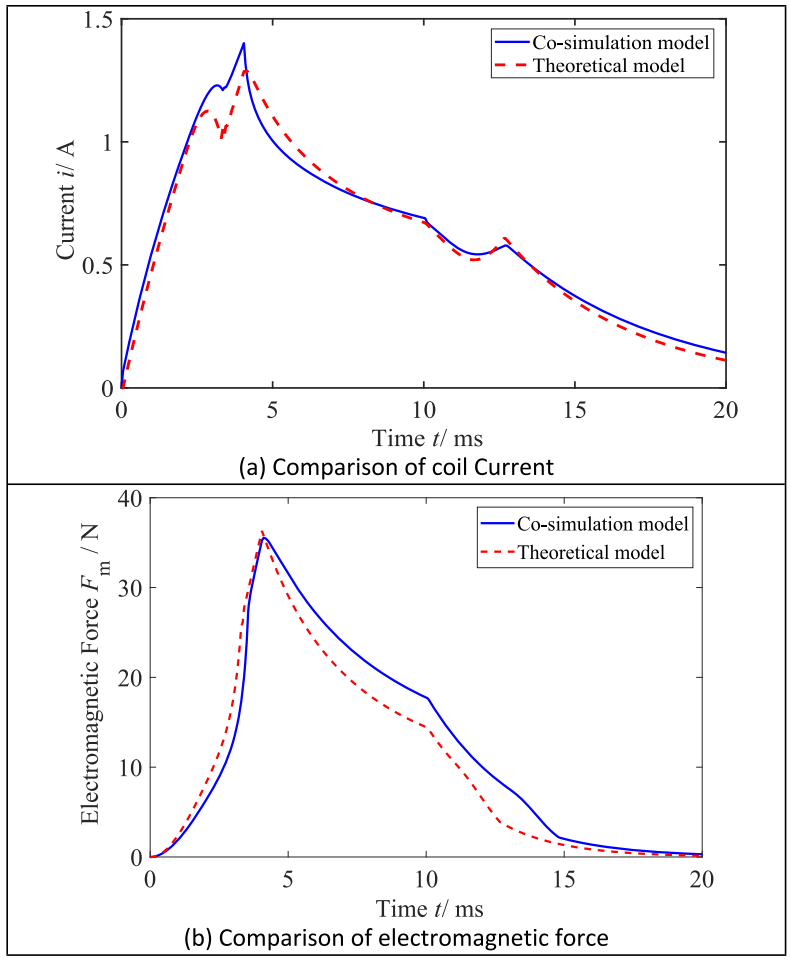

Fig. 14 Validation of co-simulation model

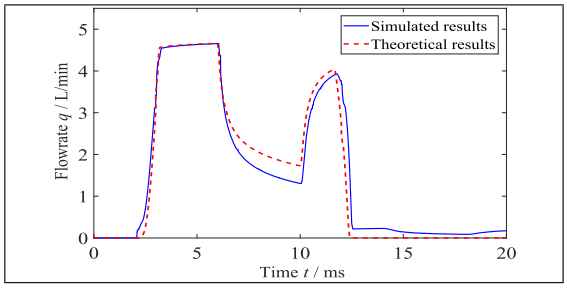

Fig. 15 Transient flowrate at the pulsation supply pressure

inactive (either in the closed state or fully open). The error in the critical opening time point between the experimental and co-simulated result is 14.8%, while the error in the fully open time point is approximately 16.1%. During the coil current discharge phase, the experimentally measured transient coil current also displays a spike (where the current initially increases and then decreases), showing a high degree of consistency with the co-simulation model. The error in the critical closing time point is approximately 6%, and the error in the fully closed time point is about 12.5%. The average error between the experimentally measured coil current and that of co-simulated is approximately 6.9%. The comparison between the calculated transient upstream pressure response, transient delivery flow rate and that of measured are depicted in Fig. 18.

As demonstrated in Fig. 18a, both experimental and theoretical results demonstrate significant pressure oscillations downstream of the high speed solenoid valve, with the pressure oscillation trends exhibiting remarkable consistency. The amplitude errors between the co-simulated and measured pressure curves not exceeding 3.7%, and response time errors within 2 ms, accounting for approximately 2%

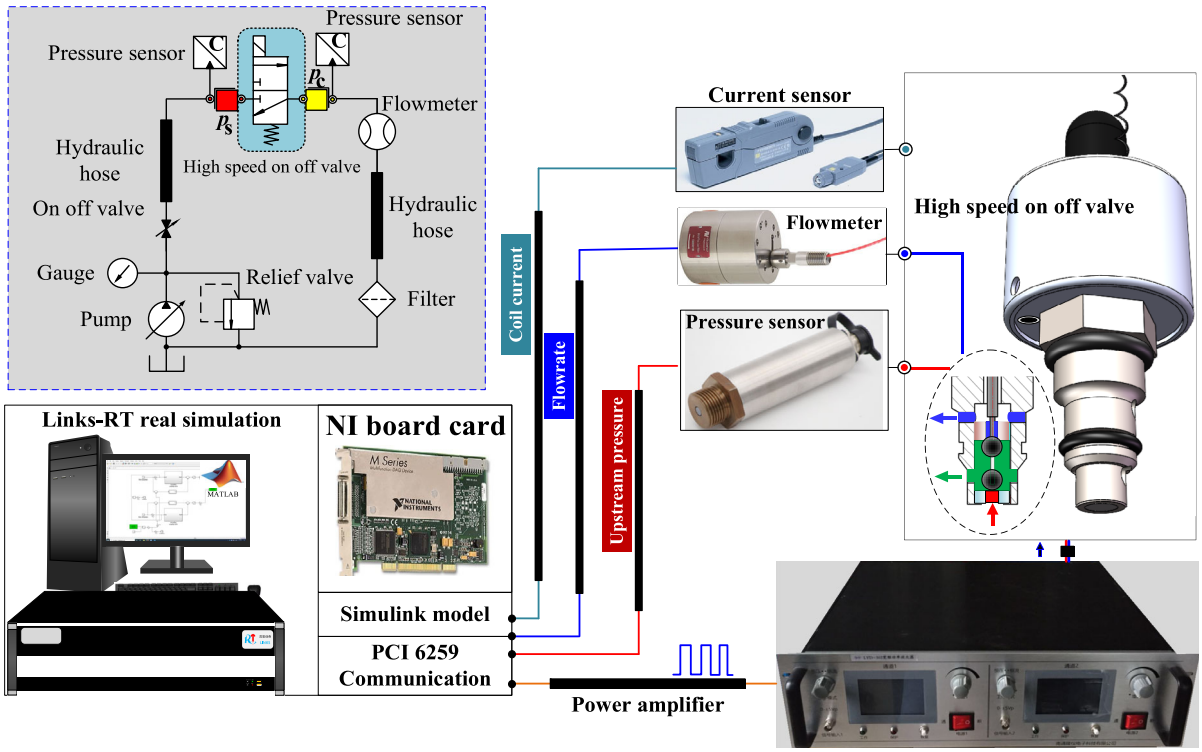

Fig. 16 Characteristic validation test rig of high speed solenoid valve

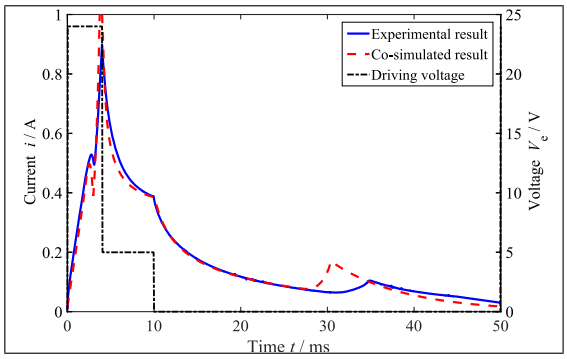

Fig. 17 Comparison of excitation current between the experimental and co-simulated result

of the high speed solenoid valve's switching frequency. Specifically, during valve opening, the peak value of the first forward pressure wave approaches 3.5 MPa, while the peak value of the first reverse pressure wave decreases to approximately 3.1 MPa. Subsequently, the pressure undergoes two complete cycles of amplitude attenuation, stabilizing at 3.25 MPa. During valve closure, the peak value of the first reverse pressure wave approaches 0 MPa, and the peak value of the first forward pressure wave reaches approximately 2.7 MPa. This is followed by 1.5 cycles of pressure amplitude attenuation, with the pressure stabilizing at 2.8 MPa.

As shown in Fig. 18b, at an operating frequency of 5 Hz, the output flow rate q_d gradually increases to 2.29 L/min when the duty ratio ranges from 0 to 0.65. When the duty ratio $\tau \geq 0.65$, the output flow rate begins to decline slowly, eventually decreasing to 0.53 L/min. Throughout the entire operating cycle, there is no flow maintenance phase, and the average output flow rate is 1.41 L/min. The flow characteristics model demonstrates excellent agreement with the experimental data, with a discrepancy between the co-simulated flow characteristics curve and the measured transient flow rate of only 0.08 L/min.

8 Conclusions

The several characteristics of high speed solenoid valve are and experiments discussed by using multi-

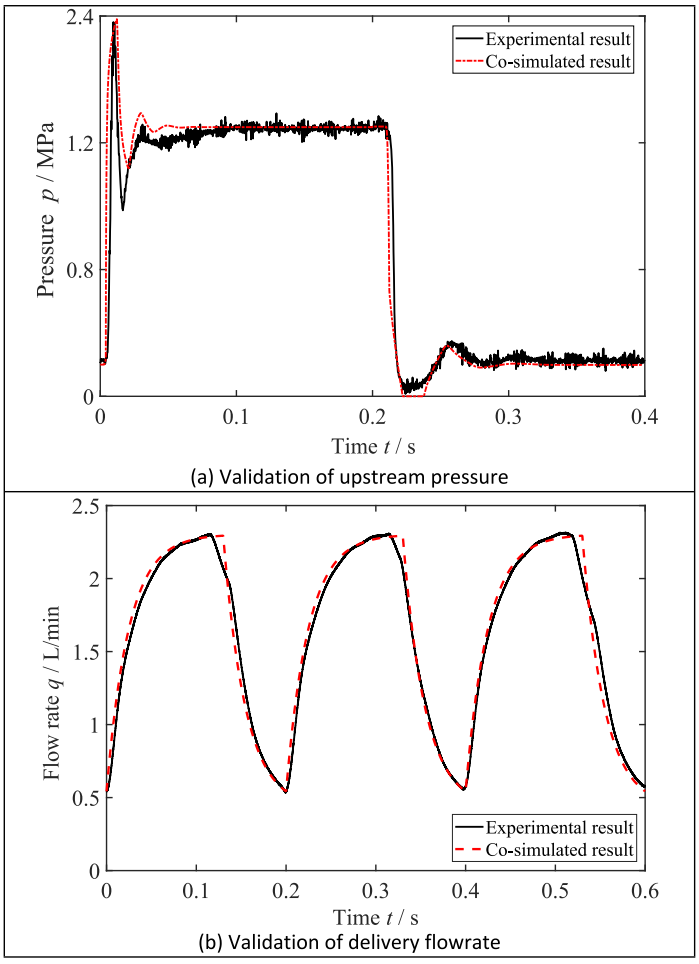

Fig. 18 Validation of transient upstream pressure and delivery flowrate

physics co-simulation model. Several primary conclusions were given as follows:

(1) The calculated results indicated that the electromagnetic force and excitation current are sensitive to the threshold air gap even its profiles due to electromagnetic field distribution incorporated into co-simulation model. The fluid-dependent force calculated in form of integral eliminates the complexity of conventional formulas, and the approximated results are acquired.

(2) The coil current calculated by the co-simulation model is consistent with that of validated theoretical model, the maximum tolerance of total opening current and time are 14% and 0.6%, respectively; the maximum tolerance of total closing current and time are 5.1% and 0.4%, respectively. As illustrated in the acquired excitation current curve, the error in the critical closing time point is approximately 6%, and the error in the fully closed time point is about 12.5%. The average error between the experimentally measured coil current and that of co-simulated is approximately 6.9%.

(3) During the single switched period, the pulsation of supply pressure enables the unsteady delivery flowrate, and the error between the theoretical model and simulated model is 0.05L/min. The amplitude errors of pressure oscillation between the co-simulated and measured pressure curves not exceeding 3.7%, and response time errors within 2 ms, accounting for approximately 2% of the high speed solenoid valve's switching frequency. The flow characteristics model demonstrates excellent agreement with the experimental data, with a discrepancy between

the co-simulated flow characteristics curve and the measured transient flow rate of only 0.08 L/min.

The future research direction, high speed solenoid valves usually employ advanced control strategies based on coil current to enhance dynamic performance, but often fail to address issues such as pressure oscillations and flow pulsations caused by these strategies. Subsequent integration of multi-dimensional data interaction through the proposed multi-physics co-simulation model in COMSOL/MATLAB software enables efficient and comprehensive evaluation of the combined effects of proposed control strategies, laying the foundation for more efficient and high-precision digital flow control in high speed solenoid valves.

Author contributions Chen Xiaoming wrote the main manuscript text and prepared Figs. 1–18. Zhu Yuchuan, Qin Cheng and Li Yangmin reviewed the manuscript.

Funding The author(s) disclosed receipt of the following financial support for the research, authorship, and/or publication of this article: This work was supported by The National Key Research & Development Program of China (Grant No. 2022YFB3206505).

Data availability No datasets were generated or analysed during the current study.

Declarations

Conflict of interest The authors declare that there is no conflict of interest.

References

1. Rannow, M.: Achieving efficient control of hydraulic systems using on/off valves. Doctoral dissertation, University of Minnesota (2016)
2. Love, L.J., Lanke, E., Alles, P.: Estimating the Impact (Energy, Emissions and Economics) of the U.S. Fluid Power Industry. Oak Ridge National Laboratory, Oak Ridge (2012)
3. Yang, H.Y., Pan, M.: Engineering research in fluid power: a review. J. ZheJiang Univ. (Eng. Sci.) **16**(6), 427–442 (2015)
4. Scheidl, R., Linjama, M., Schmidt, S.: Is the future of fluid power digital. Proc. IMechE Part I J. Syst. Control Eng. **226**(6), 721–723 (2012)
5. Messner, F., Scheidl, R.: Development of a dual supply H-bridge amplifier for high speed actuation of digital hydraulic switching valves. Int. J. Fluid Power **20**(1), 125–150 (2019)
6. Gao, Q., Zhu, Y.C., Wu, C.W., et al.: Development of a novel two-stage proportional valve with a pilot digital flow distribution. Front. Mech. Eng. **16**, 420–434 (2021)
7. Roemer, D.B.: Design and optimization of fast switching valves for large scale digital hydraulic motors. Doctoral dissertation, Aalborg University (2014)
8. Lantela, T., Kajaste, J., Kostamo, J., et al.: Pilot operated miniature valve with fast response and high flow capacity. Int. J. Fluid Power **15**(1), 11–18 (2014)
9. Zhong, Q., Zhang, B., Hong, H., et al.: Three power sources excitation control strategy of high speed on/off valve based on current feedback. J. ZheJiang Univ. (Eng. Sci.) **52**(1), 8–15 (2017)
10. Gao, Q., Zhu, Y.C., Luo, Z., et al.: Investigation on adaptive pulse width modulation control for high speed on/off valve. J. Mech. Sci. Technol. **34**(4), 1711–1722 (2020)
11. Zhong, Q., Wang, X., Zhou, H., et al.: Investigation into the adjustable dynamic characteristic of the high-speed/valve with an advanced pulse width modulation control algorithm. IEEE/ASME Trans. Mechatron. **27**(5), 3784–3797 (2021)
12. Li, Q., Hao, P., Wang, J., et al.: Pulse-width-modulation-based time-delay compensation control for high-speed on/off valves. Electronics **12**(17), 3627 (2023)
13. Zhong, Q., Mao, Y.X., Xu, E.G., et al.: Fast dynamics and low power losses of high-speed solenoid valve based on optimized pre-excitation control algorithm. Therm. Sci. Eng. Prog. **47**, 102363 (2024)
14. Zhong, Q., Wang, J.X., Xu, E.G., et al.: Multi-objective optimization of a high speed on/off valve for dynamic performance improvement and volume minimization. Chin. J. Aeronaut. **37**(10), 435–444 (2024)
15. Zhong, Q., Zhou, W.H., Xu, E.A., et al.: Dynamic improvement and reliability enhancement of a high speed on/off valve based on pre-excitation soft switching control. Chin. J. Aeronaut. (2025). https://doi.org/10.1016/j.cja.2025.103492
16. Ma, D., Liu, Z.H., Gao, Q.H., et al.: Fault diagnosis of a solenoid valve based on multi-feature fusion. Appl. Sci. **12**(12), 5904 (2022)
17. Mahrenholz, J., Lumkes, J.: Analytical coupled modeling and model validation of hydraulic on/off valves. J. Dyn. Syst. Meas. Contr. **132**, 011005 (2010)
18. Tian, H., Zhao, Y.: Coil inductance model based solenoid on–off valve spool displacement sensing via laser calibration. Sensors **18**, 4492 (2018)
19. Yudell, A.C., Van de Ven, J.D.: Predicting solenoid valve spool displacement through current analysis. Int. J. Fluid Power **16**(3), 133–140 (2015)
20. Xu, E.G., Zhong, Q., He, X.J., et al.: A novel current-based identification method for dynamic performance of high-speed on/off valve. Measurement **232**, 114719 (2024)
21. Gao, Q., Zhu, Y.C., Wu, C.W., et al.: Identification of critical moving characteristics in high speed on/off valve based on time derivative of the coil current. Proc. IMechE Part I J. Syst. Control Eng. **235**(7), 1084–1099 (2021)
22. Wu, S., Zhao, X.Y., Li, C.F., et al.: Multi-objective optimization of a hollow plunger type solenoid for high speed on/off valve. IEEE Trans. Industr. Electron. **65**(4), 3115–3124 (2017)

23. Roemer, D.B., Bech, M.M., Johansen, P., et al.: Optimum design of a moving coil actuator for fast-switching valves in digital hydraulic pumps and motors. IEEE/ASME Trans. Mechatron. **20**(6), 2761–2770 (2015)
24. Yang, M.S., Zhang, J.H., Xu, B., et al.: Study on electromagnetic force of the new micro digital valve. Microsyst. Technol. **25**(6), 2399–2409 (2019)
25. Roemer, D.B., Johansen, P., Schmidt, L., et al.: Modeling of movement-induced and flow-induced fluid forces in fast switching valves. In: 2015 International Conference on Fluid Power and Mechatronics (FPM), Harbin, China, 05–07 August 2015, pp. 978–983
26. Meng, A.H., Gao, X., Li, N.N., et al.: Study on the effect of structural parameters on the linear control performance of high speed on-off valve based on flow field analysis. SAE Technical Paper 1644 (2020)
27. Wang, P., Kudzma, S., Johnston, N., et al.: The influence of wave effects on digital switching valve performance. In: The Fourth Workshop on Digital Fluid Power (2011)
28. Han, Z., Hu, M., Zhao, J., et al.: Study on the influences of oil supply pressure and maximum opening of electromagnetic valve on upstream pressure fluctuation. Int. J. Engine Res. **22**(3), 935–948 (2021)
29. Fang, J.G., Wang, X.F., Wu, J.J., et al.: Modeling and control of a high speed on/off valve actuator. Int. J. Automot. Technol. **20**(6), 1221–1236 (2019)
30. Gao, Q.: Investigation on the transient impact characteristics of fast switching valve during excitation stage. J. Low Freq. Noise Vib. Active Control **41**(4), 1322–1338 (2022)
31. Roberts, A., Schlotter, M., Plummer, A.R., et al.: CFX/Simulink co-simulation of a wave energy converter. In: Proceedings of the Bath/ASME Conference of Fluid Power and Motion Control (FPMC2010), Bath, UK, 15–17 September 2010
32. Yuan, X.J., Ling, H.T., Chen, J.J., et al.: A dynamic modelling method for an electro-hydraulic proportional valve combining multi-systems and moving meshes. J. Braz. Soc. Mech. Sci. Eng. **44**(7), 304 (2022)
33. Girault, V., Raviart, P.A.: Finite Element Methods for Navier-Stokes Equations, pp. 167–204. Springer, Berlin (1986)
34. Chen, X.M., Zhu, Y.C., Luo, Z., et al.: Characteristic investigation of a magnetostrictive fast switching valve for digital hydraulic converter. Proc. IMechE Part I J. Syst. Control Eng. **235**(2), 190–206 (2021)
35. McCloy, D., Martin, H.R.: Control of Fluid Power: Analysis and Design. Ellis Horwood, Chichester (1980)
36. Krus, P., Weddfelt, K., Palmberg, J.O.: Fast pipeline models for simulation of hydraulic systems. J. Dyn. Syst. Meas. Contr. **116**(1), 132–136 (1994)
37. Johnston, N., Pan, M., Kudzma, S.: An enhanced transmission line method for modelling laminar flow of liquid in pipelines. Proc. IMechE Part I J. Syst. Control Eng. **228**(4), 193–206 (2014)
38. Wiens, T.: Modeling arbitrarily shaped liquid pipelines using a segmented transmission line model. J. Dyn. Syst. Meas. Contr. **142**(6), 064502 (2020)